

ADCP observations of edge waves off Oahu in the wake of the November 2006 Kuril Islands tsunami

Jeremy D. Bricker,¹ Sophie Munger,¹ Christine Pequignet,¹ Judith R. Wells,¹ Geno Pawlak,¹ and Kwok Fai Cheung¹

Received 13 September 2007; revised 5 October 2007; accepted 8 November 2007; published 15 December 2007.

[1] During the 2006 Kuril Islands tsunami, edge waves propagating along Oahu's south shore were observed via depth-averaged ADCP velocity and pressure data acquired in real-time by a coastal observatory at 12 m depth and 400 m offshore. Time-varying rotary-component velocity spectra obtained via wavelet analysis agree with the phase lag observed between pressure and each Cartesian velocity component, in indicating the directions of rotation and travel of progressive edge waves. Furthermore, the theoretical ratios between power in the free surface elevation and in each velocity component of edge waves, agree with those observed, and a nonlinear shallow-water model shows edge waves of various modes propagating along the shore near our observation location. Importantly, the maximum surge in sea level occurred at a time when edge waves of all constituent frequencies were superposed. **Citation:** Bricker, J. D., S. Munger, C. Pequignet, J. R. Wells, G. Pawlak, and K. F. Cheung (2007), ADCP observations of edge waves off Oahu in the wake of the November 2006 Kuril Islands tsunami, *Geophys. Res. Lett.*, 34, L23617, doi:10.1029/2007GL032015.

1. Introduction

[2] A magnitude 8.3 earthquake struck the Kuril Islands (46.607°N, 153.230°E; see Figure 1) on November 15, 2006 at 11:14:16 UTC (USGS Earthquake Hazards Program, <http://earthquake.usgs.gov/eqcenter/recenteqsww/Quakes/usvcam.php>, 2007). Six hours later, the resulting small tsunami generated surges of up to 1 m height in the Hawaiian Islands, along with strong currents that caused minor damage to small boat harbors and spurred the Pacific Tsunami Warning Center (PTWC) and local authorities to herd surfers out of the water.

[3] During this tsunami, we collected both free surface elevation and current velocity data. These data reveal the presence and importance of edge waves generated by the tsunami. Previously, *González et al.* [1995] inferred the presence of tsunami-generated edge waves by investigating wave arrival times in tide gauge data along the west coast of the U.S. However, our study is the first to present current velocity data obtained under a tsunami, and to use this data to show the presence of edge waves propagating along an island coastline.

¹School of Ocean and Earth Science and Technology, University of Hawaii at Manoa, Honolulu, Hawaii, USA.

2. Observatory Setup

[4] The Kilo Nalu (Hawaiian for “Wave-Watcher”) Near-Shore Reef Observatory (hereafter KN) is a permanent cabled coastal monitoring station that collects hydrodynamic and geochemical data [*Hebert et al.*, 2007] in real-time off the south shore of Oahu (Figure 1). This data is posted on the internet in 20 minute intervals at <http://www.soest.hawaii.edu/OE/KiloNalu/>. Deployed during November 2006 was an upward-looking RDI 1200 kHz Sentinel ADCP at 12 m depth atop a coral reef at (21.288°N, 157.865°W).

[5] The ADCP was sampling in high resolution mode, recording ensemble pressure and velocity data once per second. It recorded velocity in 25 cm bins, which extended throughout the entire water column. Accuracy in the pressure measurement was 1 cm of water, and accuracy in the depth-averaged velocity measurement was better than 0.4 cm/s.

3. Analysis

3.1. Wavelets

[6] Figure 2 (top) displays a time series of observed surface elevation $\eta(t)$, bandpassed between periods of 1.7 minutes and 87 minutes. Since tsunamis are transient phenomena with many spectral components [*Rabinovich*, 1997], we used continuous wavelet analysis [*Torrence and Compo*, 1998] to decompose $\eta(t)$ into its wavelet transform $W\eta(t, T)$ and power spectrum $S\eta\eta(t, T) = |W\eta(t, T)|^2$, where T is the dominant period of the waves in each wave train passing by KN (note that T does not denote the duration of the wave train). The complex Morlet wavelet

$$\psi(t) = \frac{1}{\sqrt{\pi}} e^{i2\pi t/T} e^{-t^2} \quad (1)$$

is narrow-banded in both t and T , so well suited to our analysis. Figure 2 (bottom) displays the resulting power spectra, for low-passed data.

3.2. Duration of the Tsunami

[7] Figure 2 shows a sudden onset of the tsunami, beginning with a wave of period $T \approx 40$ min, and quickly being joined by a broad-banded array of waves in the far-infragravity range (here referring to motions shorter than the tsunami period but longer than those infragravity motions due to ocean swell and surf beat), with periods as short as 3 minutes. The shortest waves ($T < 6$ min) continued to ring for almost 1 day, while oscillations of intermediate period ($6 \text{ min} < T < 20 \text{ min}$) showed considerable power for more than 2 days, and the longest oscillations ($20 \text{ min} < T < 40 \text{ min}$) lasted up to 3 days. Power at periods longer than

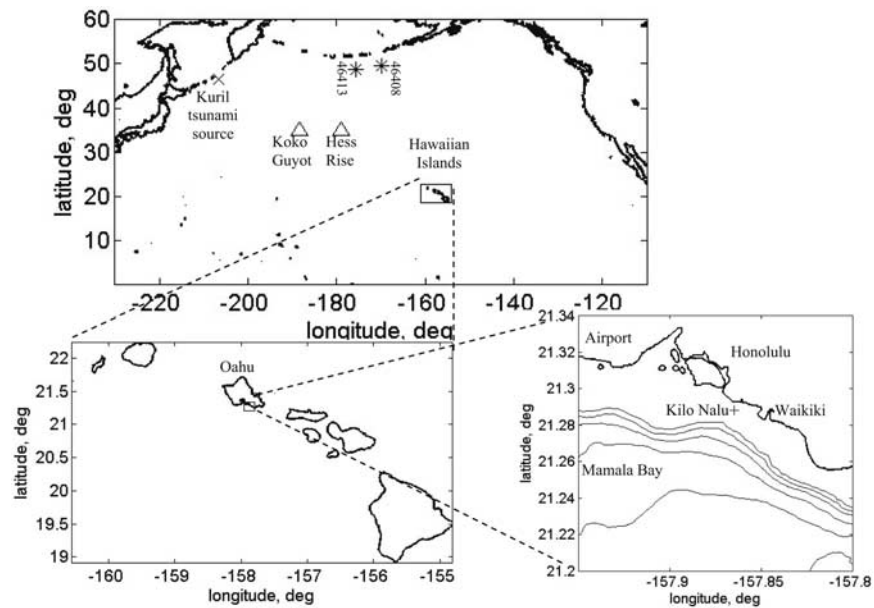


Figure 1. Maps of the Kuril Islands tsunami source (x), DART buoys (asterisks), bathymetric features (triangles), and the Kilo Nalu coastal observatory (cross). The bathymetric contour interval (light lines) on the map of Kilo Nalu is 100 m.

40 minutes corresponds to tides, which are not considered in this analysis. The works of *González et al.* [1995] and *Tinti and Vannini* [1995] infer that edge waves might be causing the far-infragravity motions, in which most of the tsunami energy at KN was contained.

3.3. Arrival of the First Wave and of the Biggest Wave

[8] Figures 3a, 3b, and 3c show $\eta(t)$, band-passed depth-averaged long-shore velocity $u_{ls}(t)$ positive to the southeast, cross-shore velocity $u_{cs}(t)$ positive seaward, and $S_{\eta\eta}(t, T)$ from the ADCP on the morning of November 15. The first ($T = 40$ min) tsunami wave hit KN at 17:43 UTC. At 18:10, far-infragravity motions with $6 \text{ min} < T < 20 \text{ min}$ arrived. Shortly thereafter, far-infragravity motions with $3 \text{ min} < T < 6 \text{ min}$ became important as well. In fact, the largest surge in

sea surface elevation occurred when maxima in power existed at all of these frequencies, at 19:15. This shows that surge height is as much affected by far-infragravity motions, as it is by long-period incident tsunami waves.

[9] Superimposed on Figure 3a is the result of a two-dimensional depth-averaged model based on the nonlinear shallow-water equations [*Wei et al.*, 2003]. The model uses earthquake source parameters adapted from the fault slip inversion computed by C. Ji (Rupture process of the 2006 Nov 15 magnitude 8.3–Kuril Island earthquake (revised), available at http://earthquake.usgs.gov/eqcenter/eqinthenews/2006/usvcam/finite_fault.php, 2007) to generate the initial conditions for the tsunami. The numerical model reproduced the tsunami waves accurately and also reproduced the initial far-infragravity

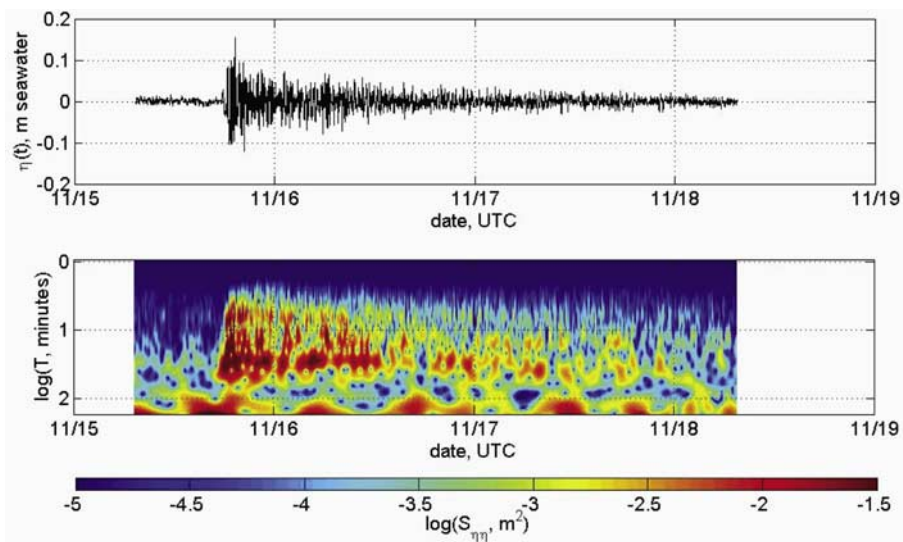


Figure 2. (top) Band-passed $\eta(t)$ at KN. (bottom) $S_{\eta\eta}(t, T)$.

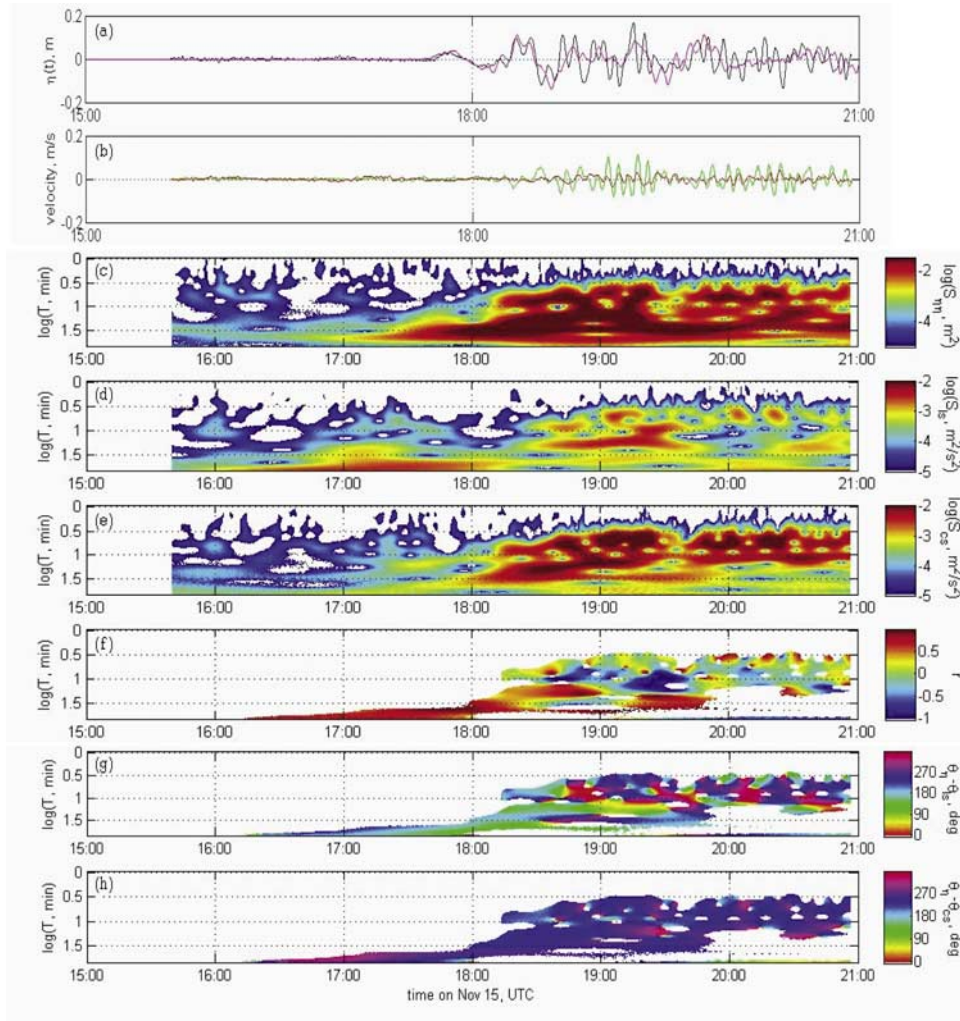


Figure 3. (a) Black, band-passed $\eta(t)$ at KN from ADCP data on November 15. Magenta, stage at KN from tsunami model. (b) Red, band-passed $u_{ls}(t)$ from ADCP data. Green, $u_{cs}(t)$. (c) $S_{\eta\eta}(t, T)$. (d) $S_{ls}(t, T)$. (e) $S_{cs}(t, T)$. (f) $r(t, T)$. (g) $\theta_{\eta}(t, T) - \theta_{ls}(t, T)$. Long-shore velocity is positive towards the southeast. (h) $\theta_r(t, T) - \theta_{cs}(t, T)$. Cross-shore velocity is positive seaward. In Figures 3f, 3g, and 3h, only data with a total power greater than $10^{-2.5} \text{ m}^2/\text{s}^2$ are shown.

motions at KN. However, after 18:30, the model no longer predicted the correct phase of the short-period motions. The model result highlights the fact that short-period motions must be modeled correctly in order to accurately predict the time and extent of the highest surge, even when incident long-period tsunami waves are modeled accurately. The discrepancy is in part due to the

approximation of the seismic source parameters and the tsunami generation mechanism, the coarse 2-min resolution used in the modeling of wave propagation across the Pacific, and the effect of dispersive short-period tsunami motions whose trans-oceanic celerity is not correctly represented by the shallow water equations.

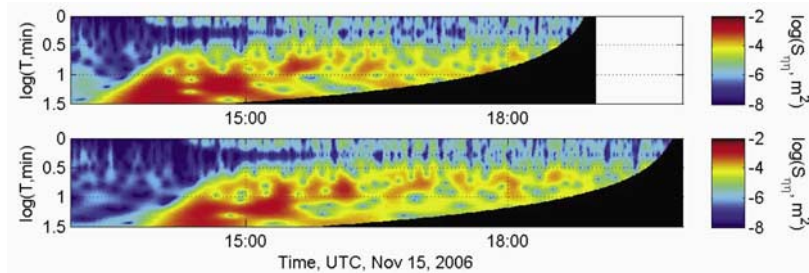


Figure 4. (top) $S_{\eta\eta}(t, T)$ at DART buoy 46413. (bottom) $S_{\eta\eta}(t, T)$ at DART buoy 46408. The black boundary is the wavelet “cone of influence” to be neglected. DART data are from NOAA National Data Buoy Center [2007].

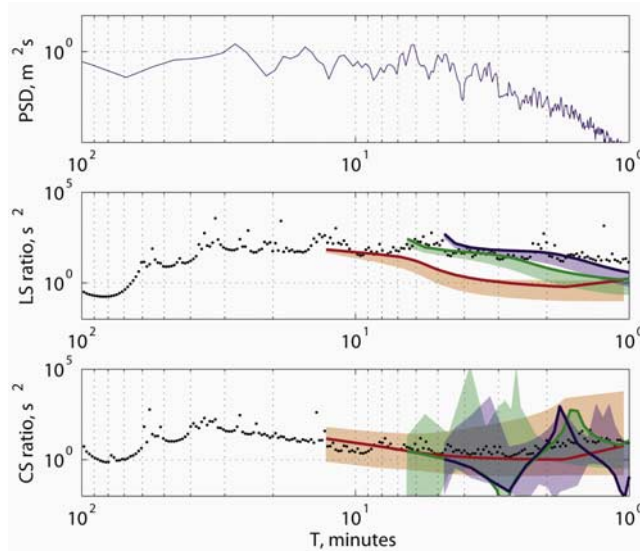


Figure 5. (top) Power spectral density of $\eta(t)$ at KN during the first 12 hours of the tsunami. (middle) Ratio of $S_{\eta\eta}$ to S_{ls} during this time. Black dots show $S_{\eta\eta}/S_{ls}$ in the data. Red line is $S_{\eta\eta}/S_{ls}$ for a theoretical mode 0 edge wave at KN. Green line is $S_{\eta\eta}/S_{ls}$ for a theoretical mode 1 edge wave. Blue line is $S_{\eta\eta}/S_{ls}$ for a theoretical mode 2 edge wave. Error patches show the full spreads in these ratios for offshore bathymetric transects at eight locations, spaced evenly between the airport and eastern Waikiki. (bottom) Ratio of $S_{\eta\eta}$ to S_{cs} . Legend same as for Figure 5 (middle) with S_{cs} replacing S_{ls} .

3.4. Delayed Arrival of Short-Period Motions

[10] As at KN, a delay between the onset of long-period motions ($T > 20$ min) and short-period motions ($T < 20$ min) existed in the open ocean, as evidenced by the DART buoy data of Figure 4 [González *et al.*, 1998; NOAA National Data Buoy Center, 2007]; this indicates that short-period motions were incident on Oahu from the deep ocean. This may be a result of the dispersive, broad-banded nature of the tsunami wave generated by the initial earthquake, or a result of trapping and scattering of the tsunami by prominent bathymetric features of the north Pacific, notably the Koko Guyot seamount and Hess Rise [Kowalik *et al.*, 2007]. Thus the edge waves we observed appear to have been generated when the short-period component of the tsunami reached Oahu from the open ocean.

3.5. Edge Waves and Rotation of the Horizontal Velocity Vector

[11] Figures 3d and 3e show power spectra $S_{ls}(t, T)$ and $S_{cs}(t, T)$ of observed depth-averaged long-shore and cross-shore velocities, respectively. Figure 3f then shows the rotary coefficient r [Gonella, 1972; Hormazabal *et al.*, 2004; Lilly and Gascard, 2006] in these velocity vectors, defined as

$$r(t, T) = \frac{S_{ccw}(t, T) - S_{cw}(t, T)}{S_{ccw}(t, T) + S_{cw}(t, T)} \quad (2)$$

where

$$S_{ccw}(t, T) = |W_{ls}(t, T)^* + iW_{cs}(t, T)|^2 \quad (3)$$

$$S_{cw}(t, T) = |W_{ls}(t, T) + iW_{cs}(t, T)|^2$$

Here, $S_{ccw}(t, T)$ is the counterclockwise (CCW) rotary-component power spectrum of velocity, $S_{cw}(t, T)$ is the corresponding clockwise (CW) power, W_{ls} is the wavelet transform of long-shore velocity, and W_{cs} is the wavelet transform of cross-shore velocity. Physically, $r = +1$ ($r = -1$) indicates a velocity vector rotating CCW (CW) in time and tracing out a circle, $r = 0$ indicates a velocity vector that varies in a rectilinear fashion, and intermediate values indicate a velocity vector tracing out an ellipse.

[12] Figure 3f shows alternating CCW and CW rotation throughout the time period of observation. Waves with $T = 16$ min have an r value that fluctuates at a rate of once per hour. Waves with $T = 6$ min have an r value that fluctuates at a rate of five cycles per hour. In edge wave theory [Ursell, 1952; Schaffer and Jonsson, 1992], a mode $n = 0$ edge wave propagating with the beach on its right (left) shows CCW (CW) rotation $r = 1$ ($r = -1$) in its horizontal velocity vector, which traces out a circle in time. A mode $n = 1$ edge wave, in the region between the beach and its offshore node, has $0 < r < 1$ ($-1 < r < 0$) when propagating with the beach on its right (left), and its horizontal velocity vector traces out an ellipse in time, with the major axis oriented in the cross-shore direction. We thus deduced that the oscillations in rotation in Figure 3f are due to progressive edge waves, alternately incident from the southeast (CCW rotation) and northwest (CW rotation).

3.6. Phase Relations and Wave Travel Directions

[13] We investigated the difference between the phase of the free surface $\theta_{\eta}(t, T)$ and that of each velocity component $\theta_{ls}(t, T)$ and $\theta_{cs}(t, T)$, where $\theta_{\eta}(t, T) = \arctan\{\text{imag}[W_{\eta}(t, T)]/\text{real}[W_{\eta}(t, T)]\}$ and similarly for $\theta_{ls}(t, T)$ and $\theta_{cs}(t, T)$. Figure 3g shows $\theta_{\eta}(t, T) - \theta_{ls}(t, T)$, while Figure 3h shows $\theta_{\eta}(t, T) - \theta_{cs}(t, T)$. At all times and periods, $\theta_{\eta}(t, T) - \theta_{cs}(t, T) \approx 270^\circ$, indicating a cross-shore standing structure with the shore in the negative cross-shore direction (as we had defined the positive cross-shore direction to be seaward). This is consistent with contributions from both progressive edge waves and standing free waves (such as a seiche).

[14] Figure 3g shows that periods of strong CCW motion (from Figure 3f) correspond to $\theta_{\eta}(t, T) - \theta_{ls}(t, T) = 180^\circ$, indicating waves with a long-shore progressive structure that are traveling in the negative long-shore direction (northwest). Such waves have the coast on their right, and are consistent with edge waves whose velocity vectors rotate CCW in time. Likewise, periods of strong CW motion correspond to $\theta_{\eta}(t, T) - \theta_{ls}(t, T) \approx 0^\circ$, indicating waves traveling in the positive long-shore direction (southeast), consistent with edge waves traveling with the coast on their left. Analyses in terms of both rotation and phase thus suggest that KN was exposed to edge waves incident from east and west.

3.7. Relation Between Pressure and Velocity

[15] We compared the ratio of $S_{\eta\eta}(t, T)$ to $S_{ls}(t, T)$ and $S_{cs}(t, T)$ in our observed data to theoretical data from a one-

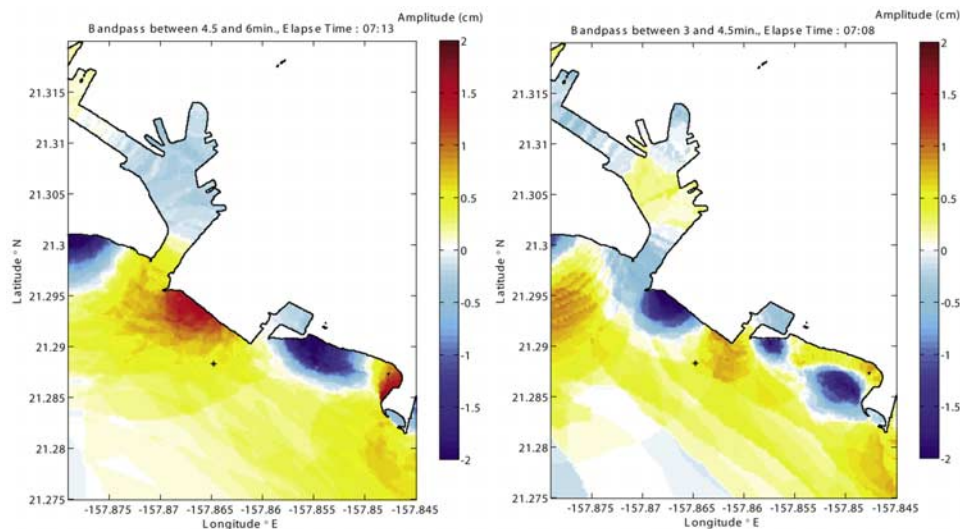


Figure 6. Snapshots of simulated sea surface height (left) at 18:31 UTC bandpassed between $4.5 \text{ min} < T < 6 \text{ min}$, and (right) at 18:26 UTC bandpassed between $3 \text{ min} < T < 4.5 \text{ min}$. KN is indicated by a dot.

dimensional edge wave model. The model applied the shallow water equations to the bathymetry off Kilo Nalu, along a transect starting at the beach and extending offshore at a heading of 210° . The model considered harmonic solutions in the long-shore direction, decaying to zero amplitude offshore, with $hu_{cs} = 0$ at the beach, where h is mean water depth. For edge waves with wavelengths between 1 km and 60 km (the length of Oahu's south shore), we solved numerically for the eigenmodes of the shallow water equations and extracted the amplitudes of η , u_{cs} , and u_{ls} at KN.

[16] Figure 5 shows the ratios of $S_{\eta\eta}(t, T)$ to $S_{ls}(t, T)$ and $S_{cs}(t, T)$ at KN, averaged over the first 12 hours of the tsunami. Error patches show the spreads in these ratios for offshore bathymetric transects at eight locations, spaced evenly between the airport and eastern Waikiki, and thus show how representative this one-dimensional model is relative to long-shore variations of bathymetry present in eastern Mamala Bay. For waves with $6 \text{ min} < T < 10 \text{ min}$, the data show agreement with mode $n = 0$ edge wave theory. At shorter periods ($T < 6 \text{ min}$), modes $n = 1$ and $n = 2$ edge waves show a better fit with the data.

[17] Figure 6 shows snapshots in time of sea surface height from the two-dimensional model of Wei *et al.* [2003] discussed above. Bandpassing the results between $4.5 \text{ min} < T < 6 \text{ min}$, we see mode $n = 0$ or $n = 1$ edge waves advecting past KN. Model results bandpassed between $3 \text{ min} < T < 4.5 \text{ min}$ show mode $n = 1$ or $n = 2$ edge waves. This is in qualitative agreement with the one-dimensional model used for Figure 5, and shows how the irregular shoreline and bathymetry of Oahu's south shore complicate the mode shapes of edge waves here.

4. Conclusions

[18] Through ADCP data from the Kilo Nalu coastal observatory, we observed far-infragravity motions near Oahu generated by trapping of short period waves from the November 2006 Kuril Islands tsunami. These motions

took the form of progressive edge waves. Edge waves were alternately traveling in both long-shore directions (east and west), indicating possible topographical generation locations in many places along the island's coastline.

[19] It is vital that simulations on which tsunami warnings are based correctly model coastal far-infragravity motions with periods as short as $T = 3 \text{ min}$ and a dispersive nature, because the superposition of these motions is what leads to the highest surges in the sea surface, and therefore the highest run-up on shore. The highest surge during our study was 17 cm, and it occurred an hour and a half after the first tsunami wave, of only 3 cm height, struck Kilo Nalu. Our data showed it to be due to the superposition of incident tsunami waves from the ocean, coastal trapped waves of various frequencies propagating along the coast, and seiches. Just as basin seiches are an important component of tsunami physics in harbors, edge waves are an important aspect of tsunami physics along the coast.

[20] **Acknowledgments.** We thank Mark Merrifield, Janet Becker, Glenn Carter, Derek Fong, Kimball Millikan and the staff of Kilo Nalu. The Kilo Nalu Observatory is supported by the National Science Foundation (grant OCE-0536616), the Office of Naval Research (grant N00014-03-1-0486) and by the UH Sea Grant College Program (institutional grant NA05OAR4171048, project R/EP-25).

References

- Gonella, J. (1972), A rotary-component method for analyzing meteorological and oceanographic vector time series, *Deep Sea Res.*, 19, 833–846.
- González, F. I., K. Satake, E. F. Boss, and H. O. Mofjeld (1995), Edge waves and non-trapped modes of the 25 April 1992 Cape Mendocino tsunami, *Pure Appl. Geophys.*, 44(3–4), 409–426.
- González, F. I., H. M. Milburn, E. N. Bernard, and J. C. Newman (1998), Deep-ocean Assessment and Reporting of Tsunamis (DART): Brief overview and status report, paper presented at the International Workshop on Tsunami Disaster Mitigation, Tokyo, 19–22 Jan.
- Hebert, A. B., F. J. Sansone, and G. Pawlak (2007), Tracer dispersal in sandy sediment porewater under enhanced physical forcing, *Cont. Shelf Res.*, 27(17), 2278–2287, doi:10.1016/j.csr.2007.05.016.
- Hormazabal, S., G. Shaffer, and O. Leth (2004), Coastal transition zone off Chile, *J. Geophys. Res.*, 109, C01021, doi:10.1029/2003JC001956.
- Kowalik, Z., J. Horrillo, W. Knight, and T. Logan (2007), The Kuril Islands tsunami of November 2006. part I: Impact at Crescent City by distant scattering, *J. Geophys. Res.*, doi:10.1029/2007JC004404, in press.

- Lilly, J. M., and J. C. Gascard (2006), Wavelet ridge diagnosis of time-varying elliptical signals with application to an oceanic eddy, *Nonlinear Processes Geophys.*, *13*, 467–483.
- NOAA National Data Buoy Center (2007), National Data Buoy Center Dart data, <http://www.ndbc.noaa.gov/dart.shtml>, Stennis Space Cent., Miss.
- Rabinovich, A. B. (1997), Spectral analysis of tsunami waves: Separation of source and topography effects, *J. Geophys. Res.*, *102*(C6), 12,663–12,676.
- Schaffer, H. A., and I. G. Jonsson (1992), Edge waves revisited, *Coastal Eng.*, *16*, 349–368.
- Tinti, S., and C. Vannini (1995), Tsunami trapping near circular islands, *Pure Appl. Geophys.*, *44*(3–4), 595–619.
- Torrence, C., and G. P. Compo (1998), A practical guide to wavelet analysis, *Bull. Am. Meteorol. Soc.*, *79*(1), 61–78.
- Ursell, F. (1952), Edge waves on a sloping beach, *Proc. R. Soc. London, Ser. A*, *214*, 79–97.
- Wei, Y., K. F. Cheung, G. D. Curtis, and C. D. McCreery (2003), Inverse algorithm for tsunami forecasts, *J. Waterw. Port Coastal Ocean Eng.*, *129*(2), 60–69.
-
- J. D. Bricker, K. F. Cheung, S. Munger, G. Pawlak, C. Pequignet, and J. R. Wells, School of Ocean and Earth Science and Technology, University of Hawaii at Manoa, 2540 Dole Street, Holmes Hall 402, Honolulu, HI 96822, USA. (pawlak@hawaii.edu)